# Thermal Neutron-Induced SEUs in the LHC Accelerator Environment

Matteo Cecchetto, Rubén García Alía, Frédéric Wrobel, Maris Tali, Oliver Stein, Giuseppe Lerner, Kacper Bilko, Luigi Esposito, Cristina Bahamonde Castro, Yacine Kadi, et al.

Matteo Cecchetto, Rubén García Alía, Frédéric Wrobel, Maris Tali, Oliver Stein, et al.. Thermal Neutron-Induced SEUs in the LHC Accelerator Environment. IEEE Transactions on Nuclear Science, 2020, 67 (7), pp.1412-1420. ⟨10.1109/TNS.2020.2997992⟩. ⟨hal-02911959⟩

# Thermal Neutron-Induced SEUs in the LHC Accelerator Environment

Matteo Cecchetto, *Student Member, IEEE*, Rubén García Alía, *Member, IEEE*,
Frédéric Wrobel, *Member, IEEE*, Maris Tali, *Member, IEEE*, Oliver Stein, Giuseppe Lerner,
Kacper Bilko, Luigi Esposito, Cristina Bahamonde Castro, Yacine Kadi, Salvatore Danzeca, *Member, IEEE*,
Matteo Brucoli, *Associate Member, IEEE*, Carlo Cazzaniga, Marta Bagatin, *Member, IEEE*,
Simone Gerardin, *Associate Member, IEEE*, and Alessandro Paccagnella

***Abstract*— In addition to high-energy hadrons, which include neutrons, protons, and pions above 20 MeV, thermal neutrons (ThNs) are a major concern in terms of soft error rate (SER) for electronics operating in the large hadron collider (LHC) accelerator at the European Organization for Nuclear Research (CERN). Most of the electronic devices still contain Boron-10 inside their structure, which makes them sensitive to ThNs. The LHC radiation environment in different tunnel and shielded areas is analyzed through measurements and FLUKA simulations, showing that the ThN fluence can be considerably higher than the high-energy one, up to a factor of 50. State-of-the-art commercial-off-the-shelf (COTS) components such as SRAM, field-programmable gate arrays (FPGA), and Flash memories of different technologies are studied to derive the expected single-event upset (SEU) rate due to ThNs, relative to the high-energy hadron contribution. We find that for the studied parts and most of the accelerator applications, ThNs are the dominating source of upsets with respect to the high energy particles yielding even to neglect the latter in some cases. Indeed, they can induce, in electronics, up to more than 90% of the total upsets. The estimation is performed also for ground-level and avionic applications, and although in general, ThNs are not the main source of SER, in Flash memories they can play the same role as high energy neutrons. Related radiation hardness assurance (RHA) considerations for the qualification of components and systems against ThNs are presented.**

***Index Terms*— Avionic, commercial-off-the-shelf (COTS), field-programmable gate array (FPGA), Flash memory, ground level, high-energy neutrons (HENs), large hadron collider (LHC), radiation hardness assurance (RHA), SRAM, thermal neutrons (ThNs).**

## I. Introduction

SINGLE-EVENT upsets (SEUs) in electronic devices to be installed in the complex of the large hadron collider (LHC) accelerator are typically associated with highly energetic particles, whereas as will be outlined in this article, thermal neutrons (ThNs) can play an equal or even dominant role for certain locations and components. Along the accelerator tunnel and the shielded areas, in which electronic components are installed, the radiation environment is mainly composed of neutrons and an additional contribution from high-energy protons and pions. Neutrons range from thermal (meV) to high (GeV) energies. Most single event effects (SEEs) are therefore due to neutrons, which above few MeV (and even below for elastic processes) can indirectly ionize the sensitive volume (SV) atoms of the device through elastic and/or inelastic reactions, depending on the initial particle energy and target material. Differently, ThNs are absorbed by the $^{10}$B isotope, still present inside the device structure, producing nuclear fission with the ejection of an alpha particle and $^{7}$Li, according to the $^{10}$B(n, $\alpha$)$^{7}$Li reaction [1]. It is worth noting that high-energy neutrons (HENs) are much less efficient in inducing boron capture and fission, because the boron capture cross section shows very large values (∼3838 barns [1]) around the thermal region of 25 meV and decreases as $E^{-1/2}$ with increasing energy. The $^{7}$Li (0.849 MeV) and especially the alpha (1.47 MeV) are then capable of ionizing the silicon atoms, the charge is collected in the SV and the SEU can be triggered. Therefore, the ThN sensitivity of electronics is due to a physical interaction with the $^{10}$B. It depends on the boron amount inside the device and on its critical charge. Although the presence of $^{10}$B has been avoided in recent technologies with the removal of Borophosphosilicate glass (BPSG), it is still present inside the electronic devices as p-doping and near the back end of line (BEOL) structure as tungsten coating for the plugs connecting the drain to the copper layers [2]–[4]. These atoms of $^{10}$B originate from the $B_2H_6$ etcher gas used to improve the adhesion of tungsten in the trench contacts [5], [6]. With the technology scaling, SV and contact size decrease and consequently the amount of $^{10}$B atoms is reduced. On the other hand, the critical charge to trigger upsets has decreased and, when lowering the supply

Manuscript received March 29, 2020; revised May 7, 2020; accepted May 15, 2020. Date of publication May 27, 2020; date of current version July 16, 2020.

Matteo Cecchetto is with CERN High energy AcceleRator Mixed field facility (CHARM), 1211 Meyrin, Switzerland, and also with the IES, UMR5214, UM/CNRS, Université de Montpellier, F-34097 Montpellier, France (e-mail: matteo.cecchetto@cern.ch).

Rubén García Alía, Maris Tali, Oliver Stein, Giuseppe Lerner, Kacper Bilko, Luigi Esposito, Cristina Bahamonde Castro, Yacine Kadi, Salvatore Danzeca, and Matteo Brucoli are with CERN, 1211 Meyrin, Switzerland.

Frédéric Wrobel is with the IES, UMR5214, UM/CNRS, Université de Montpellier, F-34097 Montpellier, France.

Carlo Cazzaniga is with ISIS Facility, STFC, RAL, OX11 0QX Didcot, U.K.

Marta Bagatin, Simone Gerardin, and Alessandro Paccagnella are with the Department of Information Engineering, University of Padua, 35131 Padova, Italy.

Color versions of one or more of the figures in this article are available online at http://ieeexplore.ieee.org.

Digital Object Identifier 10.1109/TNS.2020.2997992

voltage, the SEU rate can increase almost exponentially [7]. These two competing effects typically cancel each other out and the cross section per bit is roughly constant or slightly decreasing with the technology. However, the cross section per chip increases due to the integration and other factors, such as the actual proportion of boron, which depends on the manufacturing process. These are the reasons why ThNs are becoming a major issue for the LHC accelerator but not least for avionic, terrestrial, medical, and automotive applications. As shown in [8], evaluating the response of different CPUs and GPUs, ThNs can contribute to the ground-level failure-in-time (FIT) rate up to 59% of the total.

This article will focus on the soft error rate (SER) due to ThNs along different locations of the accelerator in comparison to that from highly energetic particles. Whereas the standard component-level qualification for accelerator parts is based on the response to high-energy (200 MeV) protons, the sensitivity to ThNs is presently not investigated on a systematic basis. The aim of this study is to outline the crucial impact that ThNs can have on accelerator applications, in comparison to those at ground level and avionics. The devices involved in this study consist of SRAM, field-programmable gate array (FPGA), and Flash memories, which have been tested in thermal and HEN facilities. Ionizing radiation and, in particular, neutron effects on NAND flash memories have been extensively studied [8]–[12]. At sea level, the error rate due to radiation in NAND flash is comparable to that induced by other mechanisms affecting reliability, such as program and read disturbs, random telegraph noise, and so on. Radiation hardness assurance (RHA) implications are discussed in addition to the analysis of the results.

## II. ENVIRONMENTS

### A. Terrestrial and Atmospheric

The HEN spectrum inside commercial aircrafts, which generally fly at 12 km of altitude, can be considered the same as outside. In contrast, ThN fluxes can be more than 10 times higher inside the plane, yielding the thermal part up to 2 times higher than the HENs. The latter are typically defined, for terrestrial and atmospheric applications, as the neutrons with $E > 10$ MeV [4]. This is due to the presence of H inside many materials such as fuel, human bodies, and equipment, which thermalizes the neutrons. Therefore, the ThN flux strongly depends also on the atmospheric humidity and on the presence of water masses. For terrestrial environments (ground level), the thermal flux is measured as 6.5 [n/cm$^2$/h] and the HEN one as 13 [n/cm$^2$/h] from the Joint Electron Device Engineering Council (JEDEC) [13], whereas inside an aircraft (12 km of altitude) the International Electrotechnical Commission (IEC) standard considers a thermal to HEN ratio of 1.1 [4]. As presented in [4], at sea level, SEUs in 90 nm SRAM are basically due to neutrons above 10 MeV, but scaling down the technology to 28 nm (microprocessor cache) up to 41% of SER is expected from ThNs. At flight altitude inside the aircraft, the SER contribution of ThNs further increases up to 60% [4]. Therefore, it seems that ThN fluxes have similar probabilities of inducing SEUs as the HENs, especially with the technology scaling.

### B. Accelerator

The present data analysis of the LHC radiation environment refers to the current machine operating at about 50 fb$^{-1}$/year [14]. With the high-luminosity LHC (HL-LHC) upgrade, the nominal annual integrated luminosity will be of 250 fb$^{-1}$/year and the radiation levels are expected to, in first approximation, scale linearly. The enormous amounts of electronic commercial-off-the-shelf (COTS) components used inside the LHC accelerator are primarily installed either inside shielded alcoves or, when the cabling length is an issue (e.g., high-speed communication and high current powering), directly in the tunnel. They are all subjected to radiation levels that can vary by a considerable amount for each location in terms of fluence and particle types. These radiation levels are mainly due to beam–beam collisions (in the interaction points) and to the interaction of the beam with collimators and the residual gas molecules inside the vacuum pipe.

Radiation levels in the tunnel and shielded areas are monitored through the RadMon v6 system as detailed in [15]. This system measures the ThN and high-energy hadron equivalent (HEHeq) fluences, the latter defined as the HEH plus the weighted contribution of the intermediate energy neutrons from 0.2 to 20 MeV [16]. The fluence measurements are performed through two embedded SRAM memories differently sensitive to HEHeq and thermals.

In order to characterize every location in which the RadMons are installed, the $R$-factor is defined as the ratio between ThN and HEHeq fluences [17]

$$R = \frac{\text{ThN}}{\text{HEHeq}}. \tag{1}$$

With this formalism, a comparable (due to the different definition of high-energy particles) $R$-factor can be calculated for the ground-level and avionic environments, yielding the values of 0.5 and 1.1, respectively. The following analysis is performed with data measurements from the tunnel and shielded alcoves, which, as will be shown, are characterized by various radiation environments.

Different levels of radiation characterize the tunnel, and its layout is subdivided into arcs and insertion regions (IRs) as detailed in [14] and illustrated in Fig. 1. There is a total of 8 arcs in the LHC, each one composed of 42 half-cells which are periodic parts of three series of dipole magnets followed by one quadrupole. They are consecutively numbered and those of interest in this study are the half-cells of the dispersion suppressor (DS) from 8 to 13 included, and the arcs from 14 to 34.

RadMons in the tunnel are normally installed below the interconnections between dipoles and quadrupoles or near-critical electronic devices, at a height of 70 cm below the beam. The arcs and DS near point 1 (P1, ATLAS) and point 5 (P5, CMS) have been analyzed with data from a total of 34 RadMons of which 11 are in the arcs and 23 in the DS. These data correspond to the 2018 proton operation and are presented in Table I, subdividing the $R$-factors

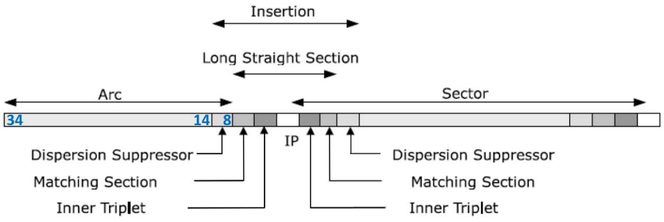

Fig. 1. LHC layout with the IR, DS from half-cells 8–13, and the arc from half-cells 14–34. The figure is adopted from [14].

TABLE I

RadMon V6 HEHeq Measurements and $R$-Factors Along the Tunnel Near Points 1 and 5 Subdivided in Three Yearly Fluence Intervals

| | $\phi_{HEHeq}$ [HEHeq/cm$^2$/year] | | | $R$-factor | | |
|---|---|---|---|---|---|---|
| area | interval | average | max | average | min | max |
| DS | $>10^9$ | $5.2\times10^{10}$ | $1.7\times10^{11}$ | 3.5 | 0.7 | 7.6 |
| ARC | $10^8$-$10^9$ | $1.6\times10^8$ | $5.2\times10^8$ | 2.7 | 2.4 | 3.0 |
| ARC | $<10^8$ | $3.6\times10^7$ | $9.1\times10^7$ | 3.4 | 1.3 | 5.7 |

into three categories: measured annual fluence greater than $10^9$ HEHeq/cm$^2$, between $10^8$ and $10^9$ HEHeq/cm$^2$, and lower than $10^8$ HEHeq/cm$^2$. The useful information is the average, minimum, and maximum $R$-factor values, and since these measurements in P1 and P5 yield compatible results, the data from the two points are merged. The highest fluences ($>10^9$ HEHeq/cm$^2$/year) are mainly in the DS, more precisely in the cells 8, 9, 11, and 13 and, as shown in Table I, the respective $R$-factors have a range of one order of magnitude, from a very low ThN contribution (0.7) to a considerable one (7.6) with respect to the HEHeq. If considering only cell 8, for which the 2018 levels were relatively large due to the debris collimator settings, the neutron fluence results in $1.7 \times 10^{11}$ HEHeq/cm$^2$/year, the maximum one recorded among all the cells (as in Table I) with a corresponding average $R$-factor of 4.6. The intermediate fluence values between $10^8$ and $10^9$ HEHeq/cm$^2$/year come from only two entries. The fluences below $10^8$ HEHeq/cm$^2$/year are measured along the LHC arcs. Their average $R$-factor is comparable with that of the high fluences in the DS, but with a minor spread. These average $R$-values are compatible, within the uncertainties, to the FLUKA simulations shown in Fig. 2 for a typical cell in the arc. FLUKA is a Monte Carlo code described in [18] and [19], which permits simulations of particle–matter interactions. Below the dipole interconnections (MBx), where the RadMons for this analysis are installed, the simulated $R$-factor is 5.2. As a summary remark, the radiation environment in the tunnel is characterized by a large spread between the $R$-factors and by relatively large average and maximum values, significantly larger than for standard ground and avionic applications.

Alcoves in the proximity of an interaction point can be heavily shielded (200 cm of cast iron/concrete), such as UJ (junction) and UL (liaison), with 98% of particles composed of neutrons, or lightly shielded (40 cm of cast iron/concrete), such as RR, with a neutron contribution varying from 70% to 90% [20]. These percentages refer to HEH fluences that are mainly composed of neutrons, protons, and pions, above 20 MeV.

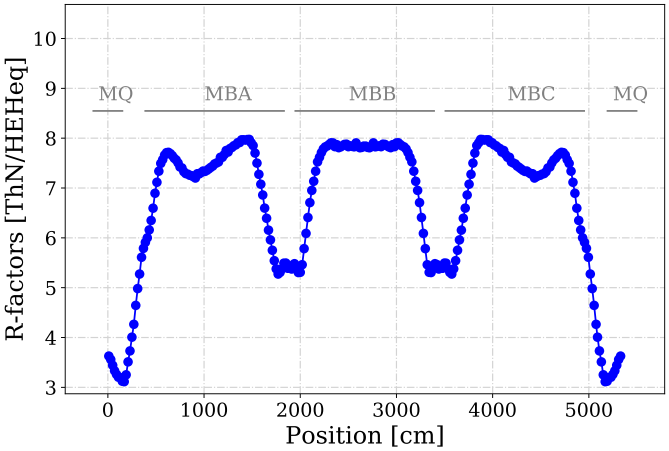

Fig. 2. FLUKA-simulated $R$-factors along cell 20, composed of three dipoles (MBx) and the quadrupole (MQ). RadMons are installed among the interconnections.

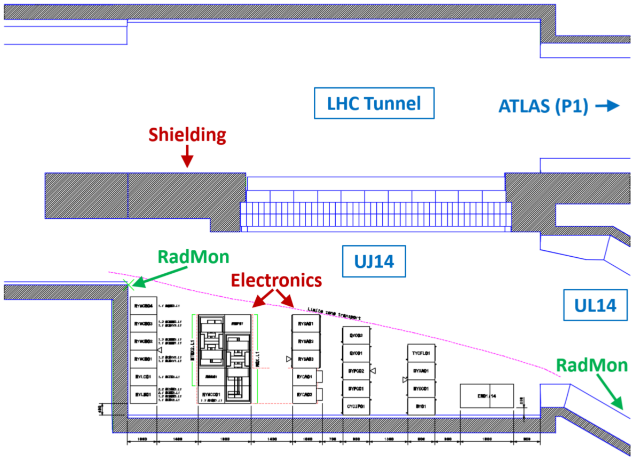

Fig. 3. UJ14 and UL14 planimetry, with the thick iron-concrete shielding separating the tunnel from the alcove in which the electronic racks are placed. RadMons are installed at positions where the fluences are expected to be the highest and the lowest.

RadMons in the shielded areas are typically installed on the concrete wall separating the tunnel from the alcove or on the ceiling among the electronic racks. In some cases, an additional device is placed in the tunnel near the shielding for fluences comparison. To give a relevant example, Fig. 3 shows the planimetry of UJ14, a heavily shielded alcove in the proximity of P1. Fig. 4 depicts the same location with a variety of machine components in the tunnel (to the left) and the concrete shielding to protect the electronics in the alcove (to the right). As can be seen in Fig. 3, the electronic racks are disposed perpendicularly to the tunnel and the RadMon is placed near the entrance (which cannot be completely closed for safety reasons), where the fluence is expected to be higher, and on the opposite side in UL14, where the fluence is expected to be lower. It is to be noted that the most sensitive equipment in the UJs was relocated to the ULs during the Long Shutdown 1 (LS1, 2013–2014) owing to the lower radiation levels. The RRs, however, still host a vast quantity of electronic racks for critical systems.

$R$-factor measurements for the alcoves in P1 and P5 are presented in Table II. While the UJs and the ULs are at several

TABLE II

*R*-FACTORS FOR THE ALCOVES IN P1 AND P5 DURING 2018. P1 IS IN BETWEEN UJ14 AND UJ16, WHICH ARE SYMMETRIC ALCOVES AS RR13 AND RR17. THE SAME APPLIES IN P5 FOR RR53 AND RR57

| Alcove | RadMon position | $R$ | $\phi_{HEHeq}$ [HEHeq/cm$^2$/y] | Point |
|---|---|---|---|---|
| RR13 | TUNNEL | 1.3 | $2.3\times10^9$ | p1 |
| RR13 | LEV0 | 9.6 | $1.6\times10^8$ | p1 |
| RR13 | LEV1 | 5.0 | $3.2\times10^8$ | p1 |
| UJ14 | LEV0 | 52.5 | $2.7\times10^8$ | p1 |
| UL14 | LEV0 | 18.4 | $1.3\times10^7$ | p1 |
| UJ16 | LEV0 | 44.6 | $2.7\times10^8$ | p1 |
| UL16 | LEV0 | 31.0 | $1.0\times10^7$ | p1 |
| RR17 | LEV0 | 11.1 | $1.6\times10^8$ | p1 |
| RR17 | LEV1 | 4.5 | $3.2\times10^8$ | p1 |
| RR53 | TUNNEL | 0.5 | $6.7\times10^9$ | p5 |
| RR53 | LEV0 | 4.1 | $4.0\times10^8$ | p5 |
| RR53 | LEV1 | 1.3 | $8.8\times10^8$ | p5 |
| RR57 | TUNNEL | 0.5 | $5.3\times10^9$ | p5 |
| RR57 | LEV0 | 5.7 | $3.3\times10^8$ | p5 |
| RR57 | LEV1 | 2.7 | $6.6\times10^8$ | p5 |

tens of meters of distance from the experiments, the RRs are 250 m away from them and consist in two level floors (LEV0 and LEV1), both parallel to the tunnel, of which LEV0 is at the same level as the accelerator beam. As can be seen, ThNs in the RR tunnel side have similar fluxes as the HEH and the *R*-factor significantly increases by almost a factor of 10 inside the alcoves, especially in those at the same tunnel level. The thermal contribution is even higher inside the UJs: up to 52 times the HEHeq in the proximity of the alcove entrance. This is due to the fact that highly energetic neutrons are thermalized by the shielding. Moreover, the relative ThN fluxes decrease when moving toward the ULs. Finally, the respective HEHeq yearly fluences inside both the UJ and UL alcoves are about one order of magnitude lower than in the tunnel. This aspect has strong implications for electronic components sensitive to thermals, as will be shown hereafter.

The simulated neutron spectra for the alcove UJ16 and the corresponding tunnel are shown in Fig. 5 in the unit of lethargy per 250 fb$^{-1}$ of luminosity, in logarithmic scale. As can be seen, the shielded alcove reduces the flux by about 3 orders of magnitude. Three different peaks can be distinguished: those corresponding to thermal (around 25 meV), evaporation (1 MeV), and spallation (100 MeV) neutrons. To better observe the ThN contribution, Fig. 6 shows the same lethargy graph in linear scale (thus, with the areas below the curves representing the integral fluxes in the different energy ranges), with the tunnel spectrum values divided by a factor 1000 in order to overlap the two HEH parts. Two effects are now more evident: the HEH flux is almost negligible compared to the thermal peak and the neutron thermalization when passing from the tunnel to the alcove. Flux and energy are reduced by the concrete and iron shielding resulting in a relatively higher flux of ThNs.

Fig. 4. Photograph of UJ14. The tunnel to the left just before the ATLAS experiment and the shielded alcove to the right.

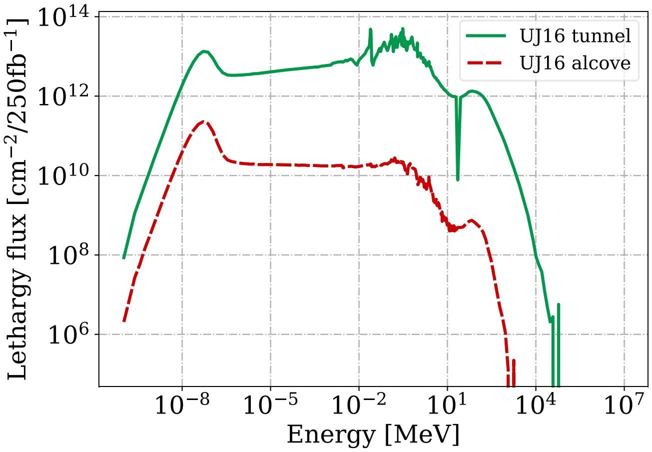

Fig. 5. FLUKA simulated neutron spectrum in the UJ16 shielded alcove and in the adjacent LHC tunnel. Both axes are in logarithmic scale.

Moreover, the simulated *R*-factors can be computed from these spectra. For this, the ThN and HEHeq fluences are obtained by folding the spectra with the inverse square root of the energy and the Weibull fit of the SRAM (the one sensitive to HEH) embedded in the RadMon, respectively. Inside the alcove, the simulated *R*-factor results 32.3, while it is around 1 in the adjacent tunnel. Considering the fact that the scoring region in the FLUKA simulation of UJ16 is just behind the shielding with a volume of 12 × 2 × 1 m, while the RadMon is confined in a much smaller volume ($R = 44.6$ from Table II), and the thermal spectrum strongly depends on the exact location and material composition, the two *R*-values are compatible.

## III. COMPONENTS AND FACILITIES

Three types of COTS devices are considered for the tests and the subsequent analysis: SRAMs, FPGAs, and Flash memories. In addition, the ESA SEU Monitor [21] is employed as a rad-hard golden chip composed of a 16-Mbit SRAM from Atmel (AT68166H-YM20-E1817), which has been calibrated in a large set of environments. The beam homogeneity in every facility was assessed with this reference monitor before performing the tests. The SRAM memories consist of a 40-nm ISSI (IS61WV204816BLL-10TLI), a 90 nm Cypress 8 Mbit (CY62157EV30LL-45ZSXI), and a 90 nm Cypress 16 Mbit (CY62167EV30LL-45ZXA). They were measured

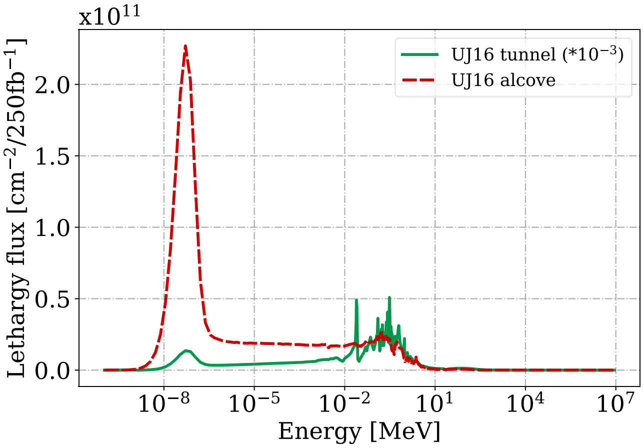

Fig. 6. FLUKA simulated neutron spectrum in the UJ16 shielded alcove and in the adjacent LHC tunnel. The $y$-axis is in linear scale and the tunnel spectrum is divided by a factor 1000 in order to overlap the two spectra above 0.1 MeV.

TABLE III

THN AND HEH SEU CROSS SECTIONS USED IN THE ANALYSIS FOR THE TESTED MEMORIES AND THEIR RATIO. THE SIZE IS EXPRESSED IN MBIT (M) OR GBIT (G)

| Memory | Tech [nm] | Size | Facility | $\sigma_{\text{HEH}}$ [cm$^2$/bit] | $\sigma_{\text{ThN}}$ [cm$^2$/bit] | Ratio |
|---|---|---|---|---|---|---|
| ESA M. | 250 | 16M | PSI, ILL | $2.6\times10^{-14}$ | $3.4\times10^{-15}$ | 7.7 |
| ISSI | 40 | 32M | ChipIr, ILL | $9.7\times10^{-15}$ | $3.2\times10^{-15}$ | 3.1 |
| Cypress | 90 | 8M | ChipIr, ILL | $5.7\times10^{-14}$ | $5.8\times10^{-16}$ | 99 |
| Cypress | 90 | 16M | ChipIr, ILL | $4.0\times10^{-14}$ | $3.9\times10^{-16}$ | 102 |
| Artix7 | 28 | 1.4M | LPSC, ILL | $9.7\times10^{-15}$ | $3.3\times10^{-15}$ | 3.0 |
| MLC Flash | 50 | 4G | LPSC, ILL | $7.1\times10^{-17}$ | $2.1\times10^{-16}$ | 0.3 |
| MLC Flash | 25 | 8G | LPSC, ILL | $2.6\times10^{-16}$ | $5.2\times10^{-16}$ | 0.5 |
| MLC Flash | 20 | 16G | LPSC, ILL | $8.6\times10^{-16}$ | $1.1\times10^{-16}$ | 8.0 |
| SLC Flash | 25 | 32G | LPSC, ILL | $4.2\times10^{-18}$ | $1.5\times10^{-19}$ | 28 |

Fig. 7. Irradiation with the SRAM tester at the ChipIr facility.

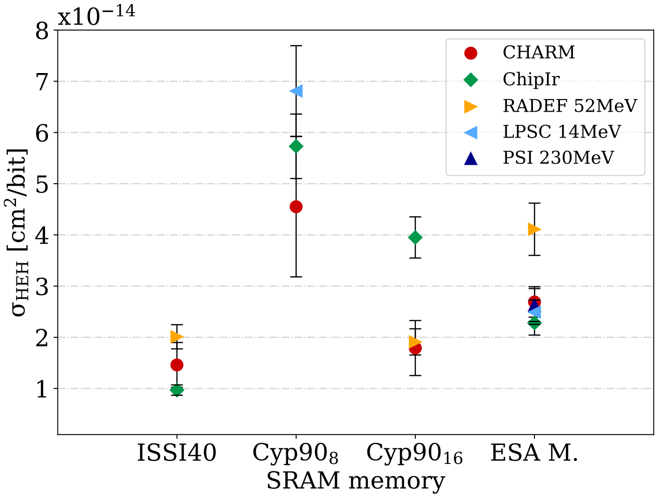

Fig. 8. HEH cross section comparison obtained in different monoenergetic/spallation facilities for the three SRAM memories. Total error bars (accounting for statistical and fluence uncertainties) are reported for $1-\sigma$.

in the different facilities by means of a motherboard tester developed at CERN, which permits to easily change the type of memory. The memory is initially written with a checkboard pattern and the reading is performed every few seconds. The data of every address are compared to the initial pattern and every bit mismatch is counted as an upset and subsequently corrected. All SRAMs were powered (on the memory pins) at 3.3 V. The FPGA is the 28 nm Artix-7 (Xilinx) from [22] powered at 1 V. The Flash memories from Micron are of different NAND technologies of 20, 25, and 50 nm. Their internal structure can be in multiple-level cell (MLC) or single-level cell (SLC) as shown in Table III. The memories were programed before the test and read after the irradiation. A reference sample not irradiated was considered in order to subtract the possible errors not due to the irradiation. The Flash memories were measured before and after irradiation at the University of Padova.

The involved test facilities were the Laboratoire de Physique Subatomique et de Cosmologie (LPSC) [23] and the D50 instrument at the Institut Laue-Langevin (ILL) [24] in Grenoble, providing 14 MeV and ThNs, respectively. In addition, the CERN High energy AcceleRator Mixed field facility (CHARM) at CERN [25] and the Chip Irradiation (ChipIr) in the U.K. [26] were employed. CHARM resembles the radiation environments found in the LHC, producing a mixed field mainly composed of neutron and proton spectra up to several GeV. At CHARM, both HEH and ThN cross sections can be retrieved, by performing two differential measurements with and without a shielding of boron carbide, a ThN absorber, as further explained in [16]. ChipIr provides an atmospheric-like neutron spectrum up to 700 MeV, and a photograph of the beamline with the installed SRAM tester can be seen in Fig. 7.

## IV. EXPERIMENTAL RESULTS

In order to study the ThN contribution to the overall SEU count, the thermal and HEH cross sections have to be measured.

The HEH cross sections can be obtained in different manners, with monoenergetic neutron/proton beams [at the Paul Scherrer Institut (PSI), LPSC, and RADiation Effects Facility (RADEF)] or with a broad energy spectrum (CHARM and ChipIr). The cross section comparison between facilities is reported in Fig. 8 for the SRAM memories. Results from CHARM and RADEF can be found in [27] and those relative to the ESA Monitor in [28] and [29]. As can be seen, the cross sections are compatible within a factor of 2, which accounts for the measurement and facility calibration uncertainties. This aspect allows to consider a single cross section value representative of the HEH sensitivity of the memory. A similar reasoning can be made for the ThN cross sections, which were measured at ILL and with differential measurements at CHARM as reported in Fig. 9. They are also compatible within a factor of 2.

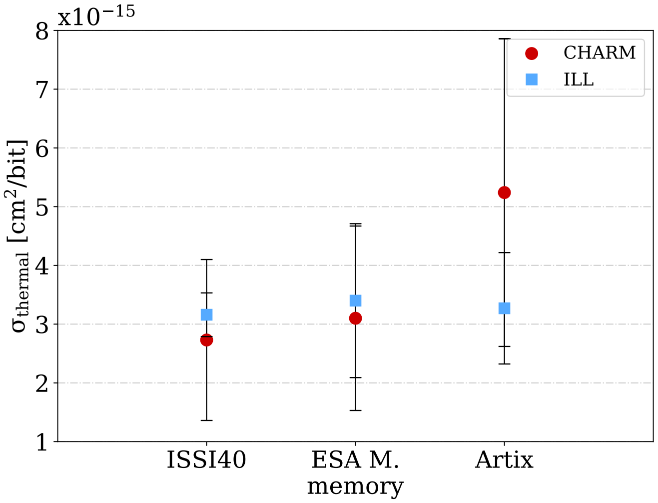

Fig. 9. ThN cross section comparison obtained at CHARM, with a differential measurement, and at ILL. Total error bars (accounting for statistical and fluence uncertainties) are reported for $1-\sigma$.

The total uncertainty on the cross sections is calculated by adding, in quadrature, two contributions: the statistical ($\sigma_{\text{stat}}$) and the fluence ($\sigma_{\text{fluence}}$) uncertainties. The statistical uncertainty derives from the measured SEUs, which can be modeled as a Poisson distribution of parameter $N$ (the number of events) with a standard deviation $\sigma_{\text{stat}} = \sqrt{N}$. As the recorded upsets during the tests were generally more than 1000, the statistical uncertainties are lower than 3%. The uncertainty on the fluence is obtained from the flux calibration of the facility and it is normally about 10% the fluence value. In addition, before every test, the beam homogeneity is evaluated through the ESA Monitor which shows the upset rate in four different dies covering a total surface of 19.8 × 19.8 mm$^2$. The relative standard error is calculated from this cross calibration and added in quadrature to the flux uncertainty provided by the facility to retrieve $\sigma_{\text{fluence}}$. Furthermore, the uncertainty accounting for the sample variations may be included. At least two samples of the same reference were tested for the Flash memories and the ESA Monitor, while for the SRAMs one sample was used. As shown in [30], for the same Cypress 8 Mbit reference, the 1-$\sigma$ standard deviation due to the sample to sample variation is calculated to be ~20%. It can be assumed a reasonable value for SRAMs and a conservative uncertainty for the other devices. The sample uncertainty would dominate the total uncertainty in ChipIr, LPSC, and RADEF, yielding the overall error bars 1-$\sigma$ within 25%.

The respective cross sections for the subsequent analysis are reported in Table III, indicating the test facilities in which they were measured. For coherence, all ThN cross sections are shown and measured at ILL. Based on these data and those from Tables I and II, the expected SEU rate, due to ThNs and HEH, is calculated for the considered critical LHC locations. As the 25 nm SLC Flash memory showed a very low ThN cross section (three orders of magnitude lower compared to the others) and almost 30 times lower than the HEH one, its thermal sensitivity can be neglected and thus it will not be included in the following analysis. In general, for the other memories, the HEH cross section is higher than the ThN one by up to 100 times for the Cypress. Although at first glance the ThN contribution might be neglected for these memories, it is of fundamental importance to know the operational environment in which they will be operating. As it will be shown, in some LHC locations, ThNs can still play a considerable role in inducing SEUs and for this reason these memories are included in the analysis. It is noticeable that for the 50- and 25-nm Flash memories, the thermal cross section is instead higher with respect to the HEH one, up to 3 times. This can occur also in SRAMs, such as the Toshiba Memory in [17], and it depends on the amount of $^{10}$B inside the device and its critical charge.

TABLE IV

EXAMPLE OF EXPECTED SEUs DUE TO ThNs AND HEH ALONG THE LHC. VALUES FOR ISSI AND ARTIX ARE IN EVENTS/YEAR/MBIT, WHEREAS IN EVENTS/YEAR/Gbit FOR THE MLC FLASH 25 nm

| Location | $N_{SEU}$ *Thermal* | | | $N_{SEU}$ *HEH* | | |
|---|---|---|---|---|---|---|
| | ISSI | Artix | Flash25 | ISSI | Artix | Flash25 |
| RR Tunnel | 10 | 10 | 1664 | 23 | 23 | 648 |
| RR | 6 | 6 | 987 | 2 | 2 | 2 |
| UJ | 47 | 47 | 7848 | 3 | 3 | 75 |
| UL | 1 | 1 | 173 | 0 | 0 | 3 |
| DS cell 8 | 1489 | 1519 | 251129 | 668 | 659 | 18489 |
| DS | 45 | 46 | 7544 | 23 | 23 | 633 |
| ARC | 1 | 1 | 138 | 1 | 1 | 18 |

The most meaningful results among the same memory type are reported in Table IV, in particular, for the ISSI 40 nm, Artix 28 nm, and the 25 nm MLC Flash memory. They express the expected absolute upset values during one year of operation, per Mbit for the SRAM and FPGA and per Gbit for the Flash memory. For the former, results are very similar because they have almost the same cross section ratio. The associated uncertainty on these values is mainly due to the uncertainty propagation from the HEH and ThN measurements of the RadMon and estimated to be up to 40% [17]. Therefore, the values are not directly comparable as the Flash memory capacity is higher. Considering all the results in units of Mbit, the Flash memories are the less sensitive (both to ThNs and HEH) with respect to SRAMs and FPGA. However, the overall SEU count per memory is hundreds of times higher for the Flash. As can be seen, the most critical areas in terms of SER are the DS cell 8 and alcove UJ for all the memories. The most important results are shown in Table V reporting the percentage of upsets caused by ThNs with respect to the HEH. The contributions are calculated for the LHC areas and compared to those expected in ground-level and avionic (inside an aircraft at 12 km of altitude) environments.

In addition, the underestimation factor $U$ is defined as the ratio between the expected events in operation (due to HEH and thermals) and those usually calculated in qualification (due to HEH) as follows:

$$U = \frac{N_{\text{oper}}}{N_{\text{qual}}} = 1 + R \cdot \frac{\sigma_{\text{ThN}}}{\sigma_{\text{HEH}}}. \tag{2}$$

The majority of qualification tests are often performed considering solely the HEH fluence contribution, neglecting the ThN one. This is acceptable if the $U$ factor is close to 1, but when higher than 2, the SER underestimation,

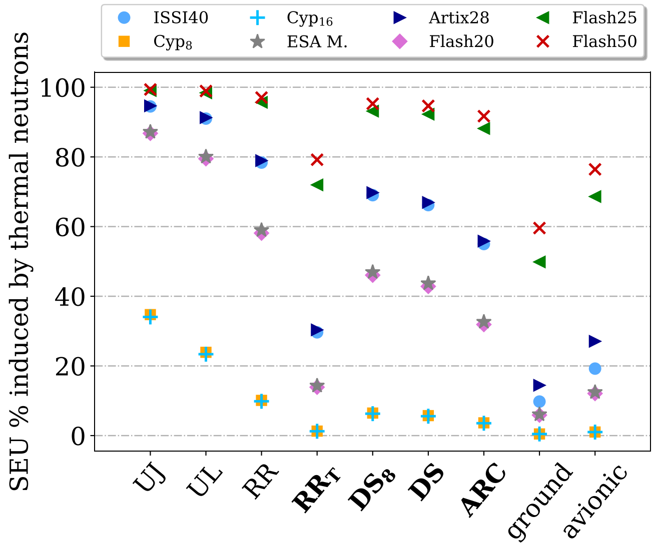

Fig. 10. Estimated SEUs (in percentage) induced by ThNs with respect to the HEH, for different LHC locations, ground, and avionic applications. $RR_T$ refers to the tunnel as well as the areas in bold. Estimated uncertainty to be up to 40%, mainly due to the RadMon fluence measurements.

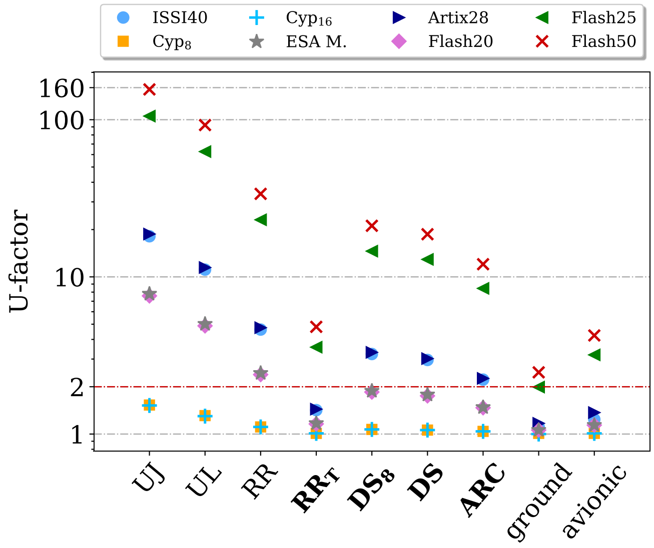

Fig. 11. U-factor for different LHC locations, ground, and avionic applications. $RR_T$ refers to the tunnel as well as the areas in bold.

TABLE V

PERCENTAGE CONTRIBUTION OF THERMALS TO THE SEUS WITH RESPECT TO THE HEH. $U$ IS THE RHA UNDERESTIMATION FACTOR. ACCELERATOR VALUES IN COMPARISON TO GROUND-LEVEL AND AVIONIC (12 km) APPLICATIONS

| Environment | ISSI 40 nm | | Artix 28 nm | | Flash$^{MLC}$ 25 nm | |
|---|---|---|---|---|---|---|
| | *ThN%* | *U* | *ThN%* | *U* | *ThN%* | *U* |
| RR Tunnel | 30 | 1.4 | 30 | 1.4 | 72 | 3.6 |
| RR | 78 | 4.6 | 79 | 4.7 | 96 | 23.1 |
| UJ | 94 | 18.1 | 95 | 18.7 | 99 | 105.4 |
| UL | 91 | 11.1 | 91 | 11.5 | 98 | 62.7 |
| DS cell 8 | 69 | 3.2 | 70 | 3.3 | 93 | 14.6 |
| DS | 66 | 3.0 | 67 | 3.0 | 92 | 12.9 |
| ARC | 55 | 2.2 | 56 | 2.3 | 88 | 8.4 |
| ground level | 10 | 1.1 | 14 | 1.2 | 50 | 2.0 |
| avionic | 19 | 1.2 | 27 | 1.4 | 69 | 3.2 |

for neglecting ThNs, is by definition also a factor higher than 2.

The overall percentage of SEUs induced by ThNs for all the studied memories is graphically depicted in Fig. 10, in which it is noticeable the very strong impact they can have on the SER. The respective $U$-factors are shown in Fig. 11.

From Table V and Fig. 10, it is evident that electronics in the shielded alcoves (RR, UJ, and UL) will mostly suffer due to ThNs, since they can provoke up to 94%, 95%, and 99% of the total upsets in the ISSI, Artix, and MLC 25 nm Flash memory, respectively. Even in the Cypress memories, which are up to 100 times less sensitive to ThNs than HEH, the former induces up to one-third of SEUs (in UJ). ThNs are also relevant throughout the LHC tunnel, with the highest contribution in cell 8 of the DS. However, in the tunnel, the impact of ThNs on the ISSI and 28 nm FPGA is comparable to the HEH one. Only on the tunnel side of the RR, the SER counts for SRAMs and FPGAs are comparable to avionic applications, which result in different factors lower than in most of the LHC (see Table V). The same memories in ground-level operation would instead present most of the issues with HEH rather than with thermals.

## V. RHA IMPLICATIONS

Based on the results presented in this article, the RHA implications for accelerator components and systems can be drawn. As the $U$ factor is basically above 2 in alcoves and most of tunnel areas, the qualification of components against ThNs has to be taken into account. Therefore, they should not be neglected, because they can be as important as the HEH. It is relevant to note that the current RHA does not include systematic ThN tests at device level.

For future applications, the ThN qualification can be carried out through three different methods.

1) Tests with a ThN beam, such as from a reactor as ILL. The advantage is given by the fact that the fluxes can be very high, implying short test periods and the certainty that the beam is solely composed of thermals without contribution of higher energy particles. On the other hand, in this case, only single components can be tested, since the beam size of these facilities is usually not suitable for board/system testing.
2) Mixed-field differential measurements at CHARM with boron carbide to retrieve the ThN and HEH cross sections, as mentioned in Section III. Both cross sections are measured in the same facility with relatively high fluxes, and as seen in Fig. 9, ThN cross sections are compatible with those measured with method 1. Furthermore, devices and systems can be tested being the irradiation room large enough to host them. However, as explained in [16], there is the need of performing the test either with two identical memories/devices at the same time or in two different runs, in order to effectuate the differential measurements with and without the boron carbide absorber.
3) Mixed-field measurements at CHARM in a specific position with a known $R$-factor (ratio between ThN

and HEH fluxes). In this case, the ThN and HEH cross sections remain unknown and only the total upset count including the two contributions is obtained. Thus, this method is suitable only for a specific $R$-factor in operation, which is compatible with that selected during the test. However, $R$-factors in CHARM can be selected to be large depending on the facility configuration and test position, and therefore be representative of the application environment. When the operational $R$-factor is known and a device/system has to be installed in that LHC location, the same $R$-factor can be reproduced in the CHARM facility, permitting its characterization for that specific environment. On the other hand, a new characterization is needed so far as the device has to operate in a different radiation environment.

The selection of one of these methods can be different based on the accelerator application and some remarks can be adduced for its comparison with space, ground level, and avionic environments. Full boards or systems can be qualified only with method 2 or 3 whenever their dimensions are larger than a few centimeters, the typical beam size in ThN facilities for which the homogeneity is acceptable. Method 2 is preferable if electronics will be installed throughout the LHC, because there will be different $R$-factors for all of which the respective SER can be calculated, whereas method 3 is enough whenever electronics will be installed in a specific location. For the accelerator, method 3 could introduce an SEU underestimation if the $R$-factor in operation is larger than that used experimentally. On the contrary, if method 3 is applied to retrieve the high-energy cross section for space applications, in which ThNs are negligible, there would be an SEU overestimation, because the radiation field at CHARM always contains a portion of thermals. It is instead applicable for ground-level and avionic applications, since there are test positions with small $R$-factors (0.5, 1) as in those environments.

## VI. CONCLUSION

Recent studies already outlined the importance of thermal neutrons (ThNs) in ground level and avionic applications, since their impact on the SER increased in sub-micron technologies. As far as the accelerator environment is concerned, ThN fluences can be tens of times higher than those of high energy particles, especially in shielded areas. The ratio between ThN and HEH fluences varies considerably along the LHC tunnel (DS, arcs) up to a factor 8 and reaches values up to 50 in the shielded alcoves (UJ, UL, and RR), significantly larger than in terrestrial applications. FLUKA simulations confirm these data in agreement with the measurements. The knowledge of the operational environment in which the device will be operating is essential, as for those locations with high thermal fluences, even if the ThN sensitivity of the memory is 1-2 orders of magnitude lower than that of HEH, the resulting SER can be not negligible. As in some of these critical areas, SEUs due to ThNs can be very large, up to 95% of the total count in SRAMs and FPGAs, consequent RHA must be accounted for the component qualification. Beside the high-energetic proton/neutron testing, ThN measurements are therefore of primary importance. The consequent qualification should be performed in thermal reactors for single components or in the CHARM mixed-field facility for components/boards/systems. In the latter, complete information about ThN and HEH cross sections can be obtained with a differential measurement using boron carbide. Otherwise, when the installation area of electronics in the LHC is known *a priori*, a single measurement, suitable for a specific thermal/HEH ratio in operation, can be performed for the qualification.

Future work related to this topic will focus on extending the number of soft error-sensitive COTS parts to a larger set of component references and types, as well as in a more thorough description of the ThN radiation-level mapping of the LHC and its injector chain. Further studies will be carried out aiming at better understanding the origin and amount of $^{10}$B in the different parts, correlating this information with SEU Monte Carlo simulations and experimental measurements.

## ACKNOWLEDGMENT

The experiments on D50 (INDU-178) at ILL and GENEPI2 at LPSC have been performed within the "Characterization Program" of the IRT Nanoelec, co-funded by the French Government in the frame of the "Program d'Investissements d'Avenir" under reference ANR-10-AIRT-05.

## REFERENCES

[1] R. C. Baumann and E. B. Smith, "Neutron-induced $^{10}$B fission as a major source of soft errors in high density SRAMs," *Microelectron. Rel.*, vol. 41, no. 2, pp. 211–218, Feb. 2001.

[2] J. L. Autran, S. Serre, S. Semikh, D. Munteanu, G. Gasiot, and P. Roche, "Soft-error rate induced by thermal and low energy neutrons in 40 nm SRAMs," *IEEE Trans. Nucl. Sci.*, vol. 59, no. 6, pp. 2658–2665, Dec. 2012.

[3] T. Yamazaki *et al.*, "Origin analysis of thermal neutron soft error rate at nanometer scale," *J. Vac. Sci. Technol. B, Nanotechnol. Microelectron., Mater., Process., Meas., Phenomena*, vol. 33, no. 2, Feb. 2015, Art. no. 020604.

[4] C. Weulersse *et al.*, "Contribution of thermal neutrons to soft error rate," *IEEE Trans. Nucl. Sci.*, vol. 65, no. 8, pp. 1851–1857, Aug. 2018.

[5] Y.-P. Fang and A. S. Oates, "Thermal neutron-induced soft errors in advanced memory and logic devices," *IEEE Trans. Device Mater. Rel.*, vol. 14, no. 1, pp. 583–586, Mar. 2014.

[6] C.-H. Kim, I.-C. Rho, S.-H. Kim, Y.-S. Sohn, H.-S. Kang, and H.-J. Kim, "Improvement of adhesion performances of CVD-W films deposited on $B_2H_6$-based ALD-W nucleation layer," *Electrochem. Solid-State Lett.*, vol. 12, no. 3, pp. H80–H83, 2009.

[7] D. Kramer *et al.*, "LHC RadMon SRAM detectors used at different voltages to determine the thermal neutron to high energy hadron fluence ratio," *IEEE Trans. Nucl. Sci.*, vol. 58, no. 3, pp. 1117–1122, Jun. 2011.

[8] D. Oliveira *et al.*, "High-energy vs. Thermal neutron contribution to processor and memory error rates," *IEEE Trans. Nucl. Sci.*, early access, Jan. 30, 2020, doi: 10.1109/TNS.2020.2970535.

[9] M. Bagatin, S. Gerardin, A. Paccagnella, and V. Ferlet-Cavrois, "Single and multiple cell upsets in 25-nm NAND flash memories," *IEEE Trans. Nucl. Sci.*, vol. 60, no. 4, pp. 2675–2681, Aug. 2013.

[10] M. Bagatin, S. Gerardin, and A. Paccagnella, "Space and terrestrial radiation effects in flash memories," *Semicond. Sci. Technol.*, vol. 32, no. 3, Feb. 2017, Art. no. 033003.

[11] S. Gerardin, M. Bagatin, A. Paccagnella, V. Ferlet-Cavrois, A. Visconti, and C. D. Frost, "Neutron and alpha single event upsets in advanced NAND flash memories," *IEEE Trans. Nucl. Sci.*, vol. 61, no. 4, pp. 1799–1805, Aug. 2014.

[12] S. Gerardin *et al.*, "Neutron-induced upsets in NAND floating gate memories," *IEEE Trans. Device Mater. Rel.*, vol. 12, no. 2, pp. 437–444, Jun. 2012.

[13] *Measurement and Reporting of Alpha Particle and Terrestrial Cosmic Ray-Induced Soft Errors in Semiconductor Devices*, Standard 89A (JESD89A), Jan. 2012.

[14] R. Garcia Alia *et al.*, "LHC and HL-LHC: Present and future radiation environment in the high-luminosity collision points and RHA implications," *IEEE Trans. Nucl. Sci.*, vol. 65, no. 1, pp. 448–456, Jan. 2018, doi: 10.1109/TNS.2017.2776107.

[15] G. Spiezia *et al.*, "A new RadMon version for the LHC and its injection lines," *IEEE Trans. Nucl. Sci.*, vol. 61, no. 6, pp. 3424–3431, Dec. 2014.

[16] M. Cecchetto, R. Garcia Alia, S. Gerardin, M. Brugger, A. Infantino, and S. Danzeca, "Impact of thermal and intermediate energy neutrons on SRAM SEE rates in the LHC accelerator," *IEEE Trans. Nucl. Sci.*, vol. 65, no. 8, pp. 1800–1806, Aug. 2018.

[17] K. Roeed *et al.*, "Method for measuring mixed field radiation levels relevant for SEEs at the LHC," *IEEE Trans. Nucl. Sci.*, vol. 59, no. 4, pp. 1040–1047, Aug. 2012.

[18] A. Ferrari, P. R. Sala, A. Fasso, and J. Ranft, *FLUKA: A Multi-Particle Transport Code*, Doc. SLAC-R-773, 877507, Dec. 2005.

[19] G. Battistoni *et al.*, "The FLUKA code: Description and benchmarking," in *Proc. AIP Conf. Proc.*, Batavia, IL, USA, 2007, pp. 31–49.

[20] K. Roed *et al.*, "FLUKA simulations for SEE studies of critical LHC underground areas," *IEEE Trans. Nucl. Sci.*, vol. 58, no. 3, pp. 932–938, Jun. 2011.

[21] R. Harboe-Sorensen *et al.*, "From the reference SEU monitor to the technology demonstration module on-board PROBA-II," *IEEE Trans. Nucl. Sci.*, vol. 55, no. 6, pp. 3082–3087, Dec. 2008.

[22] G. Tsiligiannis *et al.*, "Radiation effects on deep submicrometer SRAM-based FPGAs under the CERN mixed-field radiation environment," *IEEE Trans. Nucl. Sci.*, vol. 65, no. 8, pp. 1511–1518, Aug. 2018.

[23] M. Cecchetto *et al.*, *SEU and SEL Measurements Using 14-MeV and Thermal Neutron Beams*, document Cern-ACC-NOTE-2018-0047, Feb. 2018. [Online]. Available: https://cds.cern.ch/record/2649007?ln=en

[24] J. Beaucour *et al.*, "Grenoble large scale facilities for advanced characterisation of microelectronics devices," in *Proc. 15th Eur. Conf. Radiat. Effects Compon. Syst. (RADECS)*, Sep. 2015, pp. 312–315. [Online]. Available: http://ieeexplore.ieee.org/document/7365616/

[25] J. Mekki, M. Brugger, R. G. Alia, A. Thornton, N. C. D. S. Mota, and S. Danzeca, "CHARM: A mixed field facility at CERN for radiation tests in ground, atmospheric, space and accelerator representative environments," *IEEE Trans. Nucl. Sci.*, vol. 63, no. 4, pp. 2106–2114, Aug. 2016.

[26] D. Chiesa *et al.*, "Measurement of the neutron flux at spallation sources using multi-foil activation," *Nucl. Instrum. Meth. Phys. Res. A, Accel. Spectrom. Detect. Assoc. Equip.*, vol. 902, pp. 14–24, Sep. 2018.

[27] M. Tali, "Single-event radiation effects in hardened and state-of-the-art components for space and high-energy accelerator applications," Ph.D. dissertation, Univ. Jyväskylä, Jyväskylä, Finland, 2019. [Online]. Available: https://jyx.jyu.fi/handle/123456789/64284

[28] M. Cecchetto *et al.*, "SEE flux and spectral hardness calibration of neutron spallation and mixed-field facilities," *IEEE Trans. Nucl. Sci.*, vol. 66, no. 7, pp. 1532–1540, Jul. 2019.

[29] M. Cecchetto *et al.*, *ESA SEU Monitor Calibration*, document CERN-EDMS-NOTE-2059465, 2019. [Online]. Available: https://edms.cern.ch/document/2059465/1

[30] S. Danzeca *et al.*, "Qualification and characterization of SRAM memories used as radiation sensors in the LHC," *IEEE Trans. Nucl. Sci.*, vol. 61, no. 6, pp. 3458–3465, Dec. 2014.